AGU PUBLICATIONS

Paleoceanography

RESEARCH ARTICLE
10.1002/2016PA003024

Poorly ventilated deep ocean at the Last Glacial Maximum inferred from carbon isotopes: A data-model comparison study

L. Menviel[1,2], J. Yu[3], F. Joos[4], A. Mouchet[5,6,7], K. J. Meissner[1,2], and M. H. England[1,2]

[1]Climate Change Research Centre, University of New South Wales, Sydney, New South Wales, Australia, [2]ARC Centre of Excellence for Climate System Science, Sydney, New South Wales, Australia, [3]Research School of Earth Sciences, Australian National University, Canberra, ACT, Australia, [4]Climate and Environmental Physics, Physics Institute and Oeschger Centre for Climate Change Research, University of Bern, Bern, Switzerland, [5]Astrophysics, Geophysics and Oceanography Department, Université de Liège, Liège, Belgium, [6]Laboratoire des Sciences du Climat et de l'Environnement, IPSL-CEA-CNRS-UVSQ, Gif-sur-Yvette, France, [7]Now at Max-Planck Institute for Meteorology, Hamburg, Germany

Key Points:
- Oceanic δ^{13}C model/data comparison suggests weaker and shallower North Atlantic Deep Water at the LGM compared to the Holocene
- δ^{13}C and ventilation ages model/data comparison further suggests very weak Antarctic Bottom Water (AABW) transport at the LGM
- A poorly ventilated ocean at the LGM would contribute to enhanced deep ocean carbon storage and particularly respired carbon

Supporting Information:
- Supporting Information S1

Correspondence to:
L. Menviel,
l.menviel@unsw.edu.au

Citation:
Menviel, L., J. Yu, F. Joos, A. Mouchet, K. J. Meissner, and M. H. England (2017), Poorly ventilated deep ocean at the Last Glacial Maximum inferred from carbon isotopes: A data-model comparison study, *Paleoceanography*, *32*, 2–17, doi:10.1002/2016PA003024.

Received 23 AUG 2016
Accepted 8 NOV 2016
Accepted article online 16 NOV 2016
Published online 4 JAN 2017

Abstract Atmospheric CO_2 was ~90 ppmv lower at the Last Glacial Maximum (LGM) compared to the late Holocene, but the mechanisms responsible for this change remain elusive. Here we employ a carbon isotope-enabled Earth System Model to investigate the role of ocean circulation in setting the LGM oceanic δ^{13}C distribution, thereby improving our understanding of glacial/interglacial atmospheric CO_2 variations. We find that the mean ocean δ^{13}C change can be explained by a 378 ± 88 Gt C (2σ) smaller LGM terrestrial carbon reservoir compared to the Holocene. Critically, in this model, differences in the oceanic δ^{13}C spatial pattern can only be reconciled with a LGM ocean circulation state characterized by a weak (10–15 Sv) and relatively shallow (2000–2500 m) North Atlantic Deep Water cell, reduced Antarctic Bottom Water transport (≤10 Sv globally integrated), and relatively weak (6–8 Sv) and shallow (1000–1500 m) North Pacific Intermediate Water formation. This oceanic circulation state is corroborated by results from the isotope-enabled Bern3D ocean model and further confirmed by high LGM ventilation ages in the deep ocean, particularly in the deep South Atlantic and South Pacific. This suggests a poorly ventilated glacial deep ocean which would have facilitated the sequestration of carbon lost from the terrestrial biosphere and atmosphere.

1. Introduction

The global oceanic circulation, mainly defined by the formation of two deep water masses, North Atlantic Deep Water (NADW) and Antarctic Bottom Water (AABW), plays a significant role in setting Earth's climate through transport of heat. In addition, the interplay between oceanic circulation and biological processes sets the vertical and horizontal gradients of nutrient and carbon concentrations, which ultimately control the atmospheric CO_2 content and thus global climate. A sound understanding of the oceanic circulation at the LGM is necessary to constrain past climate change and carbon cycle.

A range of proxy reconstructions have been used to understand Atlantic oceanic circulation changes between the LGM and Holocene. It has been proposed that NADW was weaker but reached down to ~3600 m during the LGM, based on eastern Atlantic benthic foraminiferal δ^{13}C [*Sarnthein et al.*, 1994]. By contrast, western Atlantic benthic δ^{13}C [*Curry and Oppo*, 2005] and North Atlantic ^{231}Pa/^{230}Th records [*Gherardi et al.*, 2009] suggested that glacial NADW was shallower but probably as strong as today. A shoaled boundary between glacial NADW and AABW was also inferred from deep water nutrient and carbonate ion reconstructions as well as benthic foraminiferal δ^{18}O records [*Lynch-Stieglitz et al.*, 1999; *Marchitto and Broecker*, 2006; *Yu et al.*, 2008]. A statistical reanalysis of benthic δ^{13}C, Cd/Ca, and δ^{18}O, however, suggested similar volumetric extents of glacial and present-day NADW [*Gebbie*, 2014]. This is in contrast with most model-data comparisons, which suggest a shallower and weaker NADW at the LGM [*Tagliabue et al.*, 2009; *Hesse et al.*, 2011; *Menviel et al.*, 2012]. Moreover, changes in glacial AABW remain uncertain, with either weaker [*Tagliabue et al.*, 2009] or stronger LGM AABW transport [*Hesse et al.*, 2011], inferred from modeling studies.

Numerical simulations performed with coupled atmosphere-ocean general circulation models give a wide range of LGM oceanic circulation states [*Otto-Bliesner et al.*, 2007; *Weber et al.*, 2007]. The strength and extent

Table 1. Main Characteristics of LGM Experiments[a]

Symbol	NADW	AABW	SO XP	Δ C_T	Symbol	NADW	AABW	SO XP	Δ C_T
$V1, -52 \pm 53GtC$					$V2, 205 \pm 47GtC$				
V1L ∗	S	S	-	-142	V2L ∗	S	I	-	171
V1LNAoff +	Off	I	-	-19	V2LNAoff +	Off	I	-	217
V1LNAw ●	W	I	-	-22	V2LNAw ●	W	I	-	208
V1LNAwSOw ▽	I	I	-	-6	V2LNAwSOw ▽	W	W	-	212
V1LNAwSOs △	I	S	-	-75	V2LNAwSOs △	W	S	-	181
					V2LNAwSHWw ◇	W	W	-	244
V1LNAwGR ○	I	I	+9%	-17	V2LNAwGR ○	W	I	+9%	237
$V3, 351 \pm 44GtC$					$V4, 567 \pm 39GtC$				
V3L ∗	S	I	-	313					
V3LNAoff +	Off	I	-	357					
V3LNAw ●	W	I	-	346	V4LNAw ●	W	S	-	514
V3LNAwSOw ▽	W	W	-	369					
V3LNAwSHWw ◇	W	W	-	392	V4LNAwSHWw ◇	W	W	-	605
V3LNAwSOwSHWw ⋆	W	W	-	426	V4LNAwSOwSHWw ⋆	W	W	-	609
V3LSOs ⛬	S	S	-	289				-	
V3LNAwSOs △	I	S	-	320	V4LNAwSOs △	I	S	-	534
V3LNAwGR ○	W	I	+9%	357	V4LNAwGR ○	W	I	+9%	574
V3LNAwGRSOs △	I	S	+9%	343					

[a] Δ C_T indicates the difference between the late Holocene and LGM terrestrial carbon stock (Gt C) for all the experiments performed and calculated following equation (3). The mean Δ C_T and standard deviation (1σ) for each set of experiments (V1–V4) is also shown. The relative formation rates of NADW and AABW are indicated as follows: for NADW, S = strong (≥20 Sv), I = intermediate (15–20 Sv), W = weak (10–15 Sv), or Off = shutdown (2–3 Sv); for the AABW transport in the Indo-Pacific basin, S = strong (10–16 Sv), I = intermediate (8–10 Sv), and W = weak (≤7 Sv) (Table S1). All symbols are filled except experiments in which export production (SO XP) was enhanced by 9% over the Southern Ocean (56°–36°S) compared to the preindustrial control run.

of the two major water masses are usually inversely related: weaker and shallower NADW is associated with stronger AABW occupying a larger volume of the Atlantic basin. Furthermore, strong North Atlantic surface wind curl, caused by topography changes associated with the existence of a large Laurentide ice sheet [*Ullman et al.*, 2014; *Gong et al.*, 2015] or higher ocean mixing rates at low sea level [*Wunsch*, 2003], would enhance NADW formation during the LGM. Therefore, the respective strengths of glacial NADW and AABW remain poorly constrained and a topic of ongoing debate.

Here we use the isotope-enabled LOVECLIM model, the latest benthic foraminiferal $\delta^{13}C$ compilation [*Peterson et al.*, 2014], and reconstructed ventilation ages to infer the LGM oceanic circulation state and associated carbon cycle changes (Table 1). Results are further corroborated by the LGM results of a full interglacial/glacial simulation performed with the Bern3D Earth System Model of Intermediate Complexity.

2. Methods

2.1. Carbon Isotope-Enabled Earth System Model

The Earth system model LOVECLIM, used in this study, consists of a free-surface primitive equation ocean model (3°x3°, 20 depth layers), a dynamic-thermodynamic sea ice model, a spectral T21 three-level atmospheric model based on quasi-geostrophic equations of motion, and a land surface scheme [*Goosse et al.*, 2010]. LOVECLIM includes a dynamic global vegetation model (VECODE) [*Brovkin et al.*, 1997] and a marine carbon cycle model (LOCH) [*Mouchet*, 2011], both of which incorporate carbon isotopes (^{13}C and ^{14}C) [*Mouchet*, 2013; *Menviel et al.*, 2015]. Kinetic [*Siegenthaler and Munnich*, 1981] and equilibrium isotopic fractionations [*Mook et al.*, 1974] occur during air-sea carbon exchange. Carbon fractionation occurs during marine

photosynthesis [*Freeman and Hayes*, 1992] but not during $CaCO_3$ precipitation. LOVECLIM simulates today's oceanic $\delta^{13}C$ distribution in good agreement with observations [*Menviel et al.*, 2015].

2.2. Experimental Design

As the LGM was probably not an equilibrium state, we decided to equilibrate the model under 35 ka B.P. boundary conditions and then run the model transiently to 20 ka B.P., thus giving the model time to adjust. LOVECLIM was thus first equilibrated under 35 ka B.P. boundary conditions for a duration of 10,000 years with appropriate orbital parameters, Northern Hemispheric ice sheet topography and albedo [*Abe-Ouchi et al.*, 2007], an atmospheric CO_2 content of 190 ppmv, a $\delta^{13}CO_2$ of −6.46‰, and $\Delta^{14}CO_2$ of 393‰. However, by forcing the model with a lower atmospheric CO_2 content, the ocean equilibrates with the atmosphere and thus loses carbon, in contrast to the inferences of a higher glacial oceanic carbon reservoir. We corrected for this by changing the riverine flux of dissolved inorganic carbon (DIC) and alkalinity. For tracer conservation, biogeochemical tracers loss due to sedimentation is compensated by an equivalent riverine input [*Mouchet and Francois*, 1996]. During the abrupt transition to 35 ka B.P. conditions and the first 2000 years of the subsequent equilibration, the riverine input of biogeochemical tracers were imposed. This riverine flux followed the values diagnosed from the preindustrial control run, but the flux of DIC and alkalinity were equally increased in order to obtain an equilibrium with a low atmospheric CO_2 content and a high oceanic DIC concentration. After this initial 2000 year long phase, the riverine input compensates for the biogeochemical tracers loss due to sedimentation. As a result, at 20 ka B.P., the alkalinity and DIC concentrations are respectively 123 μmol/L and 96 μmol/L higher than in the preindustrial control run. Higher alkalinity content in the ocean at the LGM could be due to the ∼120 m lower sea level and associated mean salinity increase, as well as increased carbonate weathering on exposed carbonate shelves [*Munhoven*, 2002; *Vance et al.*, 2009] and a temporary carbonate burial reduction.

During the equilibration time, the flux of $\Delta^{14}C$ from the atmosphere to the ocean was diagnosed to estimate the atmospheric $\Delta^{14}C$ production rate. After the equilibration, the atmospheric $\Delta^{14}C$ production rate was set to 2.05 atoms/cm^2/s, a value consistent with present-day and Holocene $\Delta^{14}C$ production rate estimates of 1.64 to 1.88 atoms/cm^2/s [*Kovaltsov et al.*, 2012; *Roth and Joos*, 2013], a relatively high LGM $\Delta^{14}CO_2$ and uncertainties in the strength of the solar and Earth's magnetic field in the past. The fully coupled model was then run transiently from 35 to 20 ka B.P. forced with changes in orbital parameters as well as ice sheet topography and albedo but with prognostic atmospheric CO_2, $\delta^{13}CO_2$, and $\Delta^{14}CO_2$.

Since the terrestrial biosphere is depleted in ^{13}C, marine $\delta^{13}C$ anomalies can be used to reconstruct the terrestrial carbon content. Estimates range from a 330 to 700 Gt C reduction in land carbon during the LGM compared to the late Holocene [*Shackleton*, 1977; *Duplessy et al.*, 1988; *Bird et al.*, 1994; *Ciais et al.*, 2012; *Peterson et al.*, 2014]. Despite this smaller glacial terrestrial carbon reservoir, the LGM $\delta^{13}CO_2$ (−6.46‰) was similar to the preindustrial value (−6.36‰) [*Schmitt et al.*, 2012]. To simulate the impact of depleted ^{13}C terrestrial carbon release during the glaciation, at 25 ka B.P., the model is forced with low atmospheric $\delta^{13}CO_2$ values ($\delta^{13}CO_2 = -8‰, -9‰$, and −10‰ for, respectively, V2, V3, and V4) for 100 years, after which atmospheric $\delta^{13}CO_2$ is computed prognostically and recovers to a steady state value (Figure 1). A better methodology would have been to force the model with fluxes of low terrestrial $\delta^{13}C$ over the ∼100,000 years course of the glaciation, as done in *Menviel et al.* [2012], however this is not feasible with a computationally expensive three-dimensional coupled model.

Twenty-eight LGM experiments were performed with various oceanic circulation states and changes in terrestrial carbon reservoir (Tables 1 and S1). In the experiments, NADW formation was weakened by adding freshwater into the North Atlantic (from 0.05 • to 0.1 Sv +). AABW formation was varied by altering freshwater fluxes (−0.05 Sv and −0.15 Sv △, 0.05 Sv and 0.1 Sv ▽) into the Southern Ocean, by weakening the Southern Hemispheric Westerlies by 20% (◇), or both (⋆). The effect of iron fertilization was simulated by enhancing export production in the Southern Ocean between 56°S and 36°S (∘). This was done by increasing the phytoplankton growth rate, through a 40% decrease of the light half-saturation constant.

2.3. Terrestrial Carbon Changes

The equivalent change in terrestrial carbon for the 28 LGM experiments is calculated based on equilibrium atmospheric and oceanic carbon reservoirs and their isotopic signatures (Table 1). Neglecting the dilution of

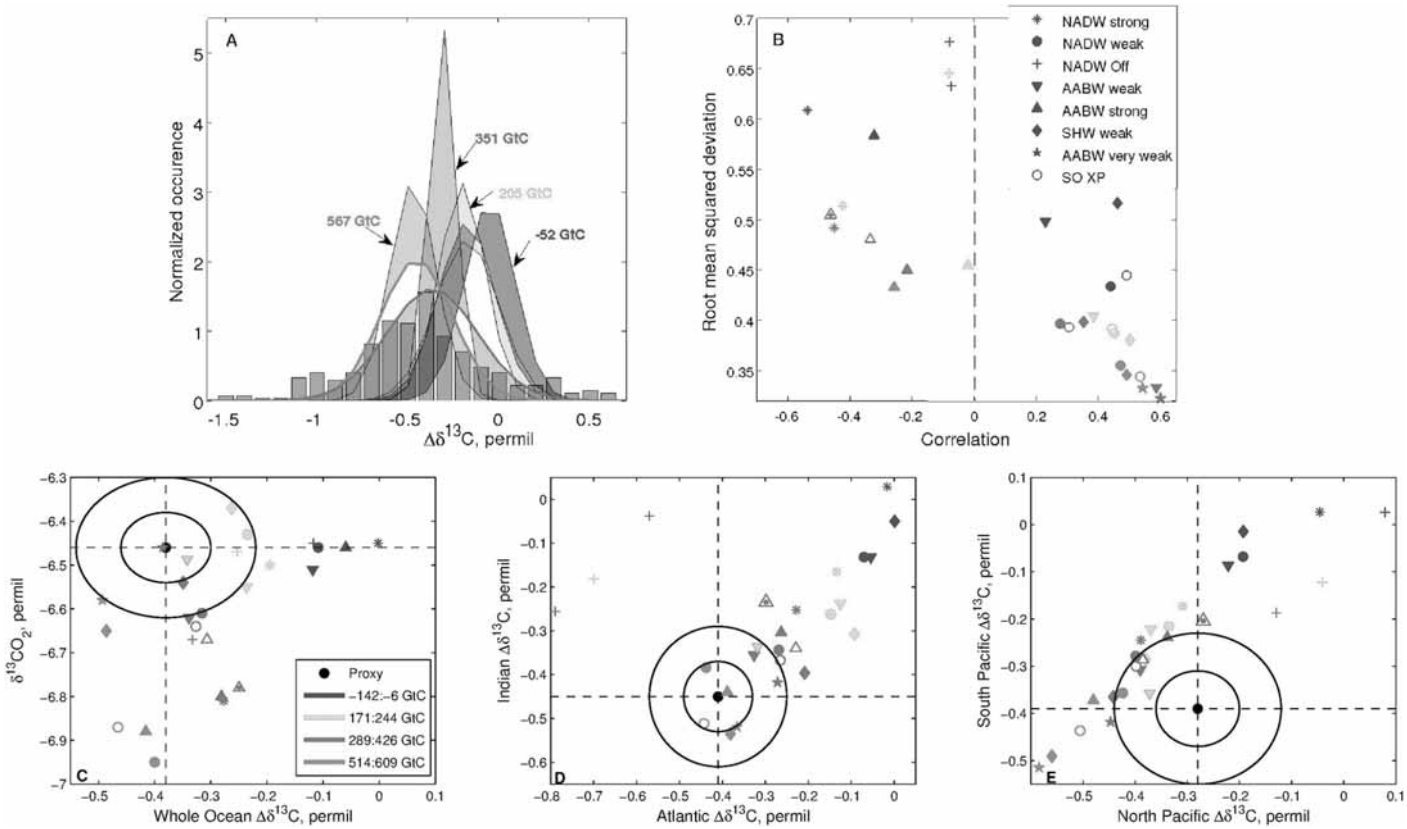

Figure 1. Simulated (colors) $\Delta\delta^{13}C$ in the LGM experiments and compared to (black) oceanic $\Delta\delta^{13}C$ [*Peterson et al.*, 2014] and atmospheric $\delta^{13}CO_2$ [*Schmitt et al.*, 2012]. (a) Probability density functions (PDF); (b) correlation versus root-mean-square deviation; (c) volume-weighted mean of the whole ocean versus atmospheric $\delta^{13}CO_2$; (d) volume-weighted mean Atlantic (55°S–77°N) versus Indian Ocean (55°S–25°N), (e) North Pacific (0°S–65°N) versus South Pacific (66°S–0°) at 0.5–5 km water depth. In Figure 1a, the thick magenta and red lines represent experiments with very weak AABW (V3LNAwSOwSHWw ⋆ and V4LNAwSOwSHWw ⋆, Table 1), and the grey bars show benthic foraminiferal $\Delta\delta^{13}C$ [*Peterson et al.*, 2014]. The color bands represent the PDF range in each group of simulations (V1–V4), without taking into account the experiments in which NADW is off (Text S3). In Figures 1c–1e, the filled orange ▽ represents an experiment performed with the Bern3D model, featuring a 340 Gt C smaller LGM terrestrial carbon stock (Text S1). Circles of radius 0.08 and 0.16‰ (1 and 2σ) are shown around the paleoproxy reconstructions. Empty symbols represent LOVECLIM experiments in which Southern Ocean export production was enhanced by 9% compared to the preindustrial control run.

an isotopic perturbation within reactive ocean sediments as well as potential changes in the weathering and burial fluxes, the conservation equation of globally integrated ^{13}C can be written as follows:

$$\begin{aligned}\int\int\int \delta^{13}C_{LA}.C_{LA}dV + \int\int\int \delta^{13}C_{LO}.C_{LO}dV + \int\int \delta^{13}C_{LT}.C_{LT}dA \\ = \int\int\int \delta^{13}C_{PA}.C_{PA}dV + \int\int\int \delta^{13}C_{PO}.C_{PO}dV + \int\int \delta^{13}C_{PT}.C_{PT}dA\end{aligned} \quad (1)$$

where $\int\int\int dV$ and $\int\int dA$ are, respectively, the volume and aerial integral of the $\delta^{13}C_{XY}$ value (‰) and C_{XY} carbon content (Gt C) of each carbon reservoir Y (A, O, and T for atmosphere, ocean, and land, respectively) at time X. The $\delta^{13}C_{XY}$ and C_{XY} are diagnosed in each experiment for the LGM (L) as well as for the preindustrial control run (P) and each grid cell of the ocean (O). We assume that the atmosphere is well mixed with a homogeneous $\delta^{13}CO_2$ value. Total preindustrial atmospheric carbon content (C_{PA}, Gt C) and mean $\delta^{13}CO_2$ ($\overline{\delta^{13}C_{PA}}$, ‰) values are diagnosed from the preindustrial control run. Total LGM atmospheric carbon content (C_{LA}, Gt C) and mean $\delta^{13}CO_2$ ($\overline{\delta^{13}C_{LA}}$, ‰) values are taken from each LGM experiment (Table S1). For the terrestrial biosphere, we consider the total simulated preindustrial carbon content and mean carbon-weighted $\delta^{13}C$ values ($\overline{\delta^{13}C_{PT}}$, $\overline{\delta^{13}C_{LT}}$). Equation (2) can then be rewritten as

$$\overline{\delta^{13}C_{PT}}.C_{PT} - \overline{\delta^{13}C_{LT}}.C_{LT} = \overline{\delta^{13}C_{LA}}.C_{LA} + \int\int\int \delta^{13}C_{LO}.C_{LO}dV - \overline{\delta^{13}C_{PA}}.C_{PA} - \int\int\int \delta^{13}C_{PO}.C_{PO}dV \quad (2)$$

The terrestrial carbon uptake from LGM to preindustrial times ($\Delta C_T = C_{PT} - C_{LT}$, Gt C) is then calculated as follows:

$$\Delta C_T = \frac{\overline{\delta^{13}C_{LA}}.C_{LA} - \overline{\delta^{13}C_{PA}}.C_{PA} + \int\int\int \delta^{13}C_{LO}.C_{LO}dV - \int\int\int \delta^{13}C_{PO}.C_{PO}dV + C_{PT}.\left(\overline{\delta^{13}C_{LT}} - \overline{\delta^{13}C_{PT}}\right)}{\overline{\delta^{13}C_{LT}}} \quad (3)$$

The simulated total preindustrial terrestrial carbon reservoir (C_{PT}) is estimated at 2050 Gt C, and the carbon-weighted mean $\delta^{13}C$ value ($\overline{\delta^{13}C_{PT}}$) is taken at −24.3‰. However, since there is some uncertainty associated with the total preindustrial carbon reservoir, we also consider a value of 2370 Gt C [*Köhler and Fischer*, 2004; *Ciais et al.*, 2012].

It has been suggested that the contribution of C4 plants relative to C3 plants was greater at the LGM, due to the low atmospheric CO_2 concentration. Since the $\delta^{13}C$ signature of C4 plants is higher than that of C3 plants, the LGM mean terrestrial $\delta^{13}C$ value ($\overline{\delta^{13}C_{LT}}$) was probably higher than the preindustrial one [*Francois et al.*, 1999]. Experiments performed with the Lund-Postdam-Jena Dynamic Global Vegetation Model (LPJ-DGVM) forced with LGM climatic boundary conditions derived from coupled general circulation models (Hadley Centre Unified Model and NCAR CSM 1.4) [*Joos et al.*, 2004] as well as PMIP-2 coupled general circulation models [*Ciais et al.*, 2012] suggest that $\overline{\delta^{13}C_T}$ was ∼1‰ higher at the LGM than during preindustrial times. We will thus take as best guess scenario $\overline{\delta^{13}C_{LT}} = -23.3$‰ but will also consider $\overline{\delta^{13}C_{LT}} = -24$‰ and −22.8‰ [*Francois et al.*, 1999; *Ciais et al.*, 2012] to quantify uncertainties in our calculations.

Since two C_{PT} values (2050 and 2370 Gt C) and three $\overline{\delta^{13}C_{LT}}$ values (−22.8‰, −23.3‰, and −24‰) are taken into account, six ΔC_T values are calculated for each LGM experiments. The mean ΔC_T values for each experiment are shown in Table 1 as well as the standard deviations of each group (V1–V4), which is similar to the standard deviation of each experiment for that group.

2.4. Statistical Analysis

The latest compilation of epibenthic foraminiferal $\delta^{13}C$ (*Cibicidoides wuellerstorfi* and related genera) is used in this study [*Peterson et al.*, 2014]. The compilation includes LGM and late Holocene $\delta^{13}C$ data from the Atlantic (Na = 246), Pacific (Np = 82) and Indian (Ni = 37) Oceans. The $\delta^{13}C$ anomalies ($\Delta\delta^{13}C$) are defined as LGM values compared to the preindustrial control experiment for the model and the late Holocene values for the proxy data. In Figures 1a and 1b, paleoproxy data [*Peterson et al.*, 2014] are linearly interpolated onto the model grid (N = 271) and the simulated $\Delta\delta^{13}C$ is resampled at each paleoproxy location. The probability density functions (PDF) of the $\delta^{13}C$ changes are computed for the proxy data and for the individual model simulations. The Pearson correlation and the root-mean-square error ($RMSE = \sqrt{\sum \frac{(m_i - d_i)^2}{N}}$) between the modeled and proxy $\Delta\delta^{13}C$ are computed for each model run to explore the overall fit and the agreement between the proxy and simulated $\Delta\delta^{13}C$ patterns. The parameters d_i and m_i, respectively, represent LGM $\Delta\delta^{13}C$ from the paleoproxy compilation [*Peterson et al.*, 2014] and as simulated by the model taken at the same locations.

To further evaluate the impact of the amount of depleted terrestrial carbon release during glaciation on oceanic $\delta^{13}C$, we calculate the volume-weighted means over ocean depths of 0.5–5 km, of the simulated LGM $\delta^{13}C$ anomalies over the whole ocean, the Atlantic (55°S–77°N), Indian (55°S–25°N), and North (0°S–65°N) and South Pacific (66°S–0°) and compare these with the estimates obtained from benthic $\delta^{13}C$ [*Peterson et al.*, 2014].

2.5. Ventilation Ages

Simulated ventilation ages in the Atlantic and Pacific Oceans are compared to available LGM ventilation ages estimates (Tables S2 and S3). Simulated ventilation ages are defined as benthic-atmosphere age differences [*Skinner et al.*, 2010; *Cook and Keigwin*, 2015], $\tau = \frac{1}{\lambda}.ln(\frac{^{14}R_{atm}}{^{14}R_{oc}})$, where the decay constant $\lambda = 1/8223$ yr^{-1} (half-life of 5700 ± 30 years) [*Bé et al.*, 2013] and $^{14}R_{atm}$ and $^{14}R_{oc}$ represent the simulated LGM $^{14}C/^{12}C$ for the atmosphere and ocean, respectively [*Ritz et al.*, 2008].

3. Results

3.1. LGM to Late Holocene Change in Terrestrial Carbon Stock

Before exploring ocean circulation changes, it is necessary to consider the global mean ocean $\delta^{13}C$ change between the LGM and the late Holocene ($\Delta\delta^{13}C$). The amount of carbon released from the low-$\delta^{13}C$ terrestrial biosphere during the glaciation controls the means of the probability density functions and the

volume-weighted $\Delta\delta^{13}C$ (Figure 1): the smaller the LGM terrestrial carbon reservoir the lower oceanic $\Delta\delta^{13}C$. However, regional changes in oceanic $\delta^{13}C$ represent a combination of mean oceanic change due to variations in the terrestrial carbon reservoir as well as changes in oceanic circulation, air-sea exchange, and export production. With constraints on the latter, which will be discussed in the following sections and are reflected in the correlation between model and proxy, regional changes in oceanic $\delta^{13}C$ can thus also inform on the mean change in terrestrial carbon, although we do acknowledge that the uncertainties are relatively large.

Simulations with an equivalent terrestrial carbon change of 205 Gt C or less (green and blue) underestimate the mean oceanic $\Delta\delta^{13}C$, while those with a change of ~570 Gt C (magenta) significantly overestimate $\Delta\delta^{13}C$ in the Pacific (Figures 1 and S4). Globally, mean simulated $\Delta\delta^{13}C$ match the proxy data the best for experiments with an average terrestrial carbon change of 351 Gt C (Figure 1 red symbols and Table 1), with our *best* simulation (V3LNAwSOwSHWw ⋆) displaying a whole ocean mean $\delta^{13}C$ change of −0.34‰. If only considering the simulations that yield a significant correlation with the benthic $\delta^{13}C$ data (Figure 1b), the best model-data agreement is obtained for experiments with a terrestrial carbon change ranging from 346 to 426 Gt C. We thus estimate that the LGM terrestrial carbon reservoir was 378 Gt C smaller than during the late Holocene (Text S2). Based on the two estimates of preindustrial total land carbon content and the three mean LGM $\overline{\delta^{13}C_{LT}}$, we estimate a one standard deviation (1σ) uncertainty of 44 Gt C for the LGM-Holocene land carbon change. This result is further confirmed by an experiment performed with the Bern3D Earth System Model, which features a 340 Gt C reduced LGM terrestrial carbon reservoir (▽, Text S1) and fits well with the proxy data (Figures 1 and S1).

3.2. North Atlantic Deep Water Formation at the LGM

Next, we attribute the spatial pattern in oceanic $\Delta\delta^{13}C$ to differences in ocean circulation between the LGM and the late Holocene. We use model-data correlation and RMSE to evaluate the match between simulations and proxy records. Paleoproxy data show a wide spread of $\Delta\delta^{13}C$ ranging from −1.85‰ to 0.6‰ (Figure 1a). Such a wide range of anomalies is expected under weak oceanic circulation, whereas a strong oceanic circulation leads to a well-mixed ocean with a narrow $\delta^{13}C$ range (Figure S2). As such, NADW cessation leads to a wide spread of $\delta^{13}C$ anomalies but negative correlations and high RMSE (Figure 1). In particular, cessation of NADW formation leads to large negative $\Delta\delta^{13}C$ (~−1‰) in the whole North Atlantic (Figure 2b), inconsistent with positive $\Delta\delta^{13}C$ reconstructions for the intermediate North Atlantic (≤2000 m water depth). Negative correlations and high RMSE are also obtained for simulations in which NADW is strong. Strong NADW formation (Figure2a) causes negative $\Delta\delta^{13}C$ at intermediate depths of the North Atlantic and little change in the entire deep Atlantic, in disagreement with paleoproxy records. The negative $\Delta\delta^{13}C$, associated with relatively high PO_4 concentrations (Figure 3) and high respired carbon content (Figure 4a) at intermediate depth in the North Atlantic, is due to (i) the relatively higher export production in the North Atlantic when NADW is strong, (ii) the strong ventilation, and associated NADW return flow, which advects very low $\delta^{13}C$, high PO_4, high respired carbon intermediate waters from the equatorial to the North Atlantic. Furthermore, strong ventilation also brings nutrient-rich, ^{13}C-depleted deep water to the surface. This $\delta^{13}C$ anomaly pattern in the North Atlantic is consistent across all the experiments featuring strong NADW (i.e., V1L, V2L, V3L, and V3LSOs, Figure S3).

When deep water formation weakens in the North Atlantic in our simulations, the NADW-AABW boundary shoals to ~2600 m compared to the preindustrial boundary of ~3300 m. Only a weakened and shoaled NADW cell leads to positive $\Delta\delta^{13}C$ above ~2000 m depth and negative anomalies below in the North Atlantic (Figures 2c–2e). This positive North Atlantic $\Delta\delta^{13}C$ is due to (i) increased fractionation between the atmosphere and surface ocean as a result of colder conditions, (ii) increased residence time at the surface of the ocean, and (iii) weaker advection of high-nutrient, low-$\delta^{13}C$ intermediate depth waters from the equatorial to the North Atlantic (Figure 3) [*Menviel et al.*, 2015]. This also results in a relatively low respired carbon content in the upper 1000 m of the North Atlantic (Figure 4d).

In agreement with the $\delta^{13}C$ model-data comparison, a shallower NADW improves the agreement between simulated and reconstructed ventilation ages in the Atlantic basin (Figure 5). Indeed, strong NADW formation leads to low ventilation ages in the deep Atlantic, in contrast with paleoreconstructions, which suggest a significantly reduced ventilation below ~2500 m in the North Atlantic [*Keigwin and Schlegel*, 2002; *Keigwin*, 2004; *Thornalley et al.*, 2011; *Skinner et al.*, 2014; *Freeman et al.*, 2016]. In addition, while the paleodata suggest a well-ventilated intermediate-depth water mass [*Freeman et al.*, 2016], a shutdown of NADW formation leads to high ventilation ages in the intermediate North Atlantic.

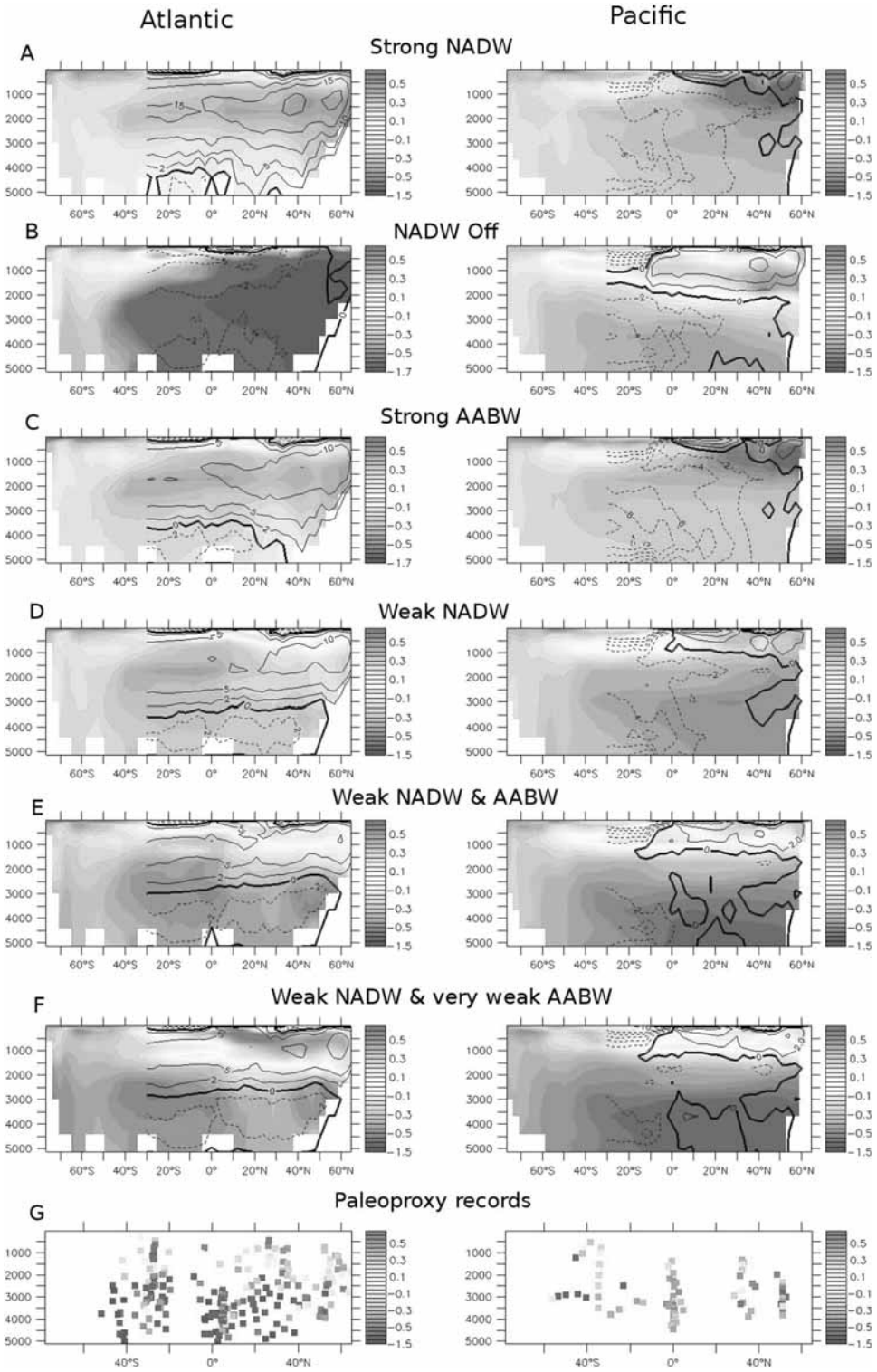

Figure 2. Meridional distributions of $\Delta\delta^{13}C$ (‰) for simulations with (a) strong NADW (V3L $*$), (b) NADW Off (V3LNAoff $+$), (c) strong AABW (V3LNAwSOs $\triangle$), (d) weak NADW (V3LNAw $\bullet$), (e) weak NADW and AABW (V3LNAwSOw $\triangledown$), and (f) weak NADW and very weak AABW obtained through both buoyancy forcing and 20% reduced Southern Hemispheric westerlies (V3LNAwSOwSHWw $\star$) compared to (g) the benthic $\delta^{13}C$ anomalies compilation [*Peterson et al.*, 2014] for (left column) the Atlantic and (right column) Pacific basins. Overlaid is the meridional overturning stream function (Sv). The LGM terrestrial carbon stock is 313 to 426 Gt C lower in these experiments.

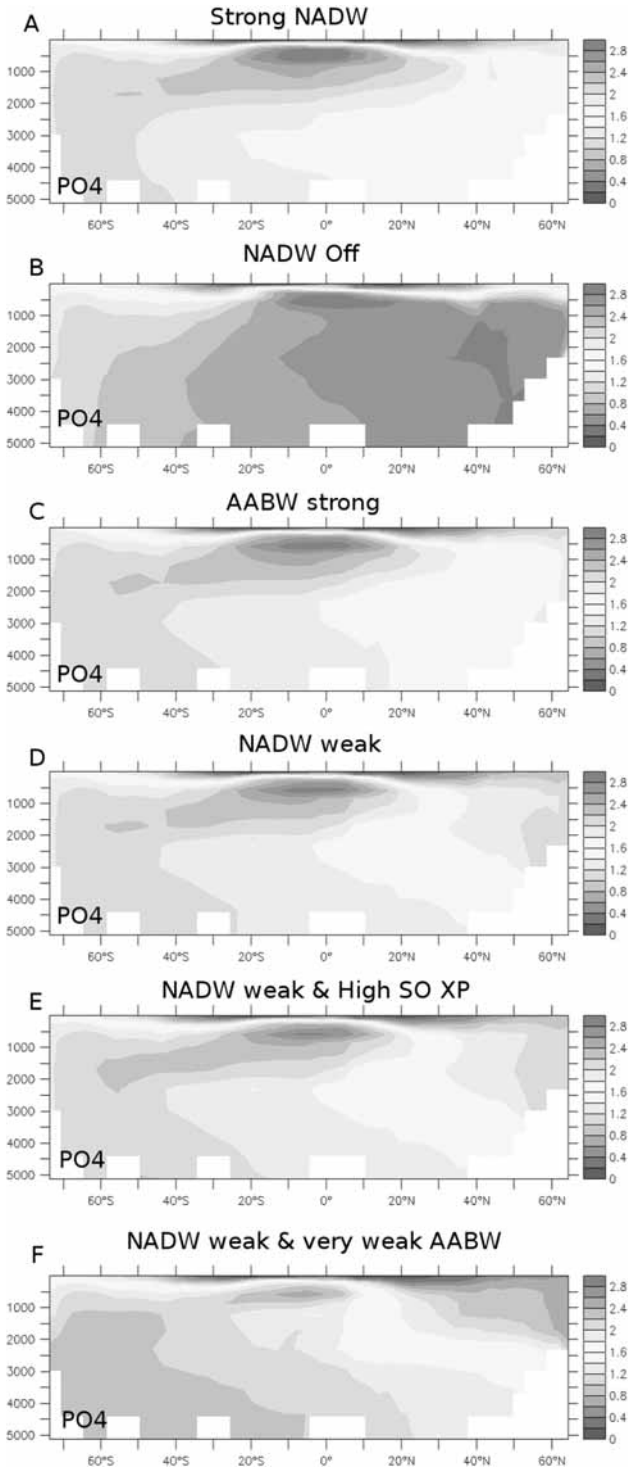

Figure 3. Phosphate content (μmol/L) zonally averaged over the Atlantic for LGM simulations with (a) strong NADW (V3L ∗), (b) NADW Off (V3LNAoff +), (c) strong AABW (V3LNAwSOs △) (d) weak NADW (V3LNAw ●), (e) weak NADW and enhanced Southern Ocean export production (V3LNAwGR ○), and (f) weak NADW and very weak AABW obtained through both buoyancy forcing and 20% reduced Southern Hemispheric westerlies (V3LNAwSOwSHWw ⋆).

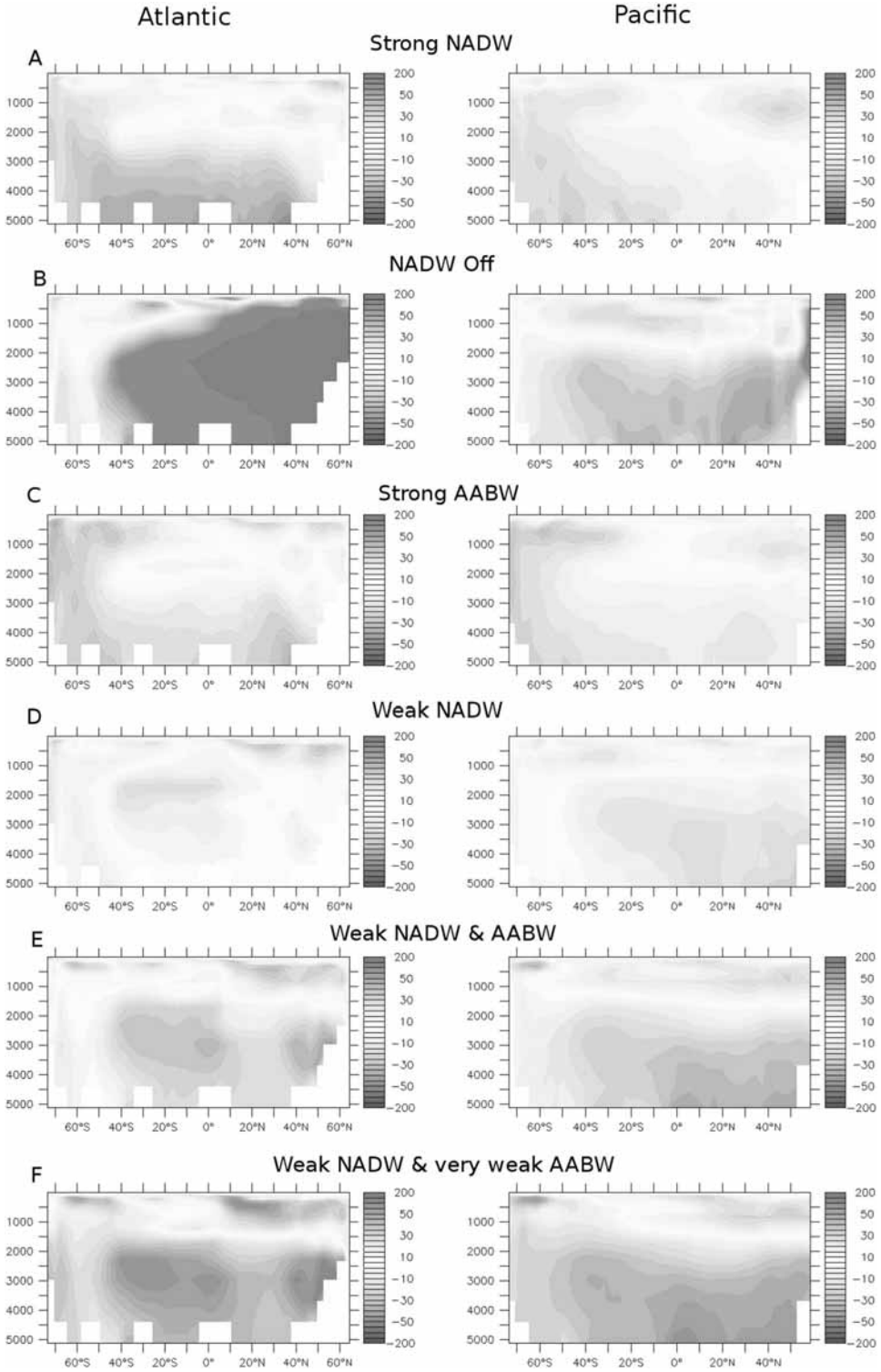

Figure 4. Respired carbon content anomalies (μmol/L, $C_{soft} = R_{C/P}{}^{*}PO_{4Rem}$) for LGM simulations compared to the preindustrial control run zonally averaged over (left column) the Atlantic and the (right column) the Pacific. LGM simulations with (a) strong NADW (V3L ∗), (b) NADW Off (V3LNAoff +), (c) strong AABW (V3LNAwSOs △), (d) weak NADW (V3LNAw ●), (e) weak NADW and weak AABW (V3LNAwSOw ▽), and (f) weak NADW and very weak AABW obtained through both buoyancy forcing and 20% reduced Southern Hemispheric westerlies (V3LNAwSOwSHWw ⋆).

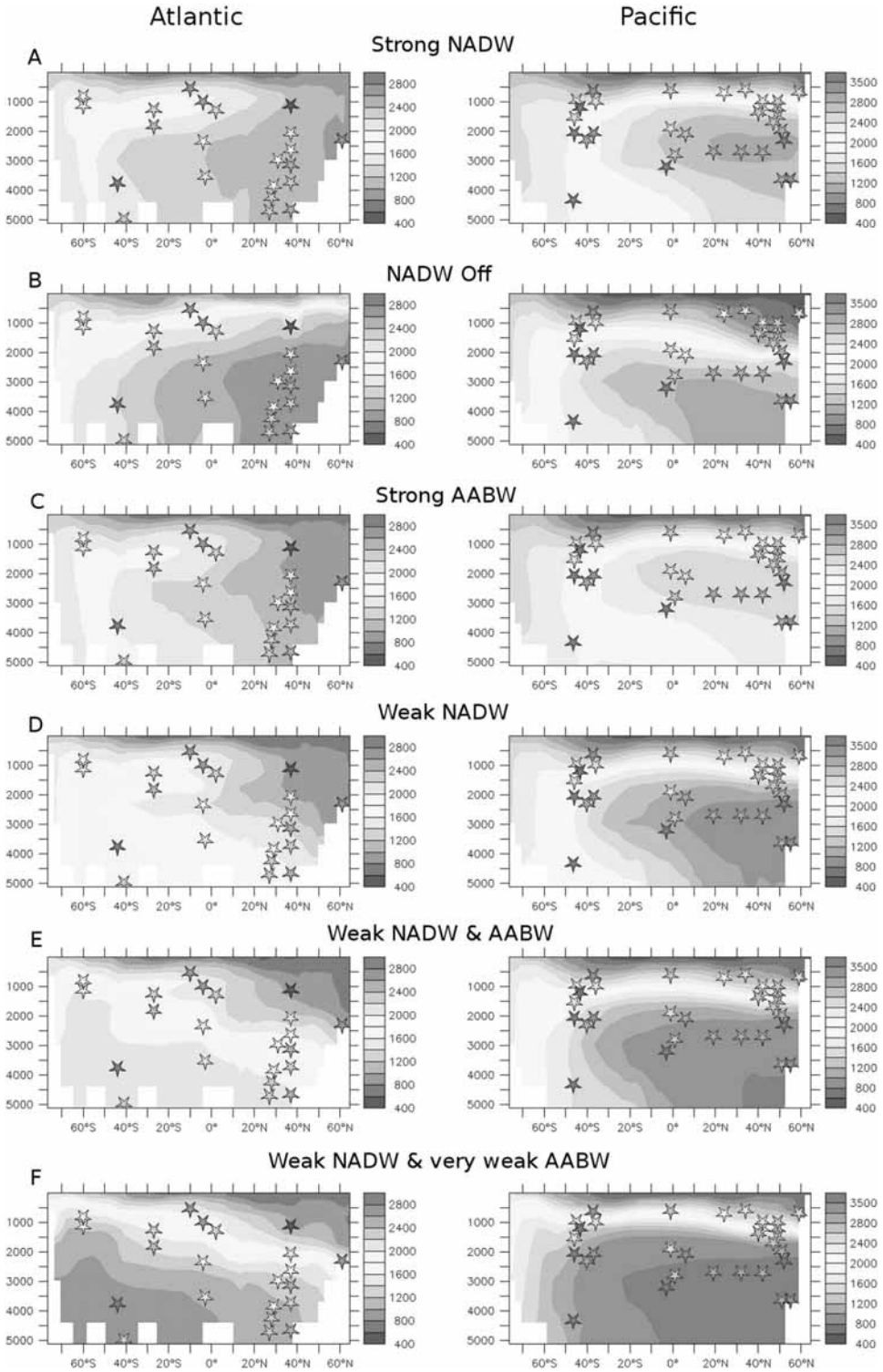

Figure 5. Ventilation age (years) for LGM simulations with (a) strong NADW (V3L ∗), (b) NADW Off (V3LNAoff +), (c) strong AABW (V3LNAwSOs △), (d) weak NADW (V3LNAw ●), (e) weak NADW and AABW (V3LNAwSOw ▽), and (f) weak NADW and very weak AABW obtained through both buoyancy forcing and 20% reduced Southern Hemispheric westerlies (V3LNAwSOwSHWw ⋆) compared to ventilation ages derived from paleoproxy records (Tables S2 and S3 [*Sikes et al.*, 2000; *De Pol-Holz et al.*, 2010; *Okazaki et al.*, 2010; *Rose et al.*, 2010; *Thornalley et al.*, 2011; *Burke and Robinson*, 2012; *Sarnthein et al.*, 2013; *Siani et al.*, 2013; *Davies-Walczak et al.*, 2014; *Rae et al.*, 2014; *Skinner et al.*, 2014; *Freeman et al.*, 2015; *Lund et al.*, 2015; *Skinner et al.*, 2015; *Freeman et al.*, 2016; *Ronge et al.*, 2016; *Weldeab et al.*, 2016]).

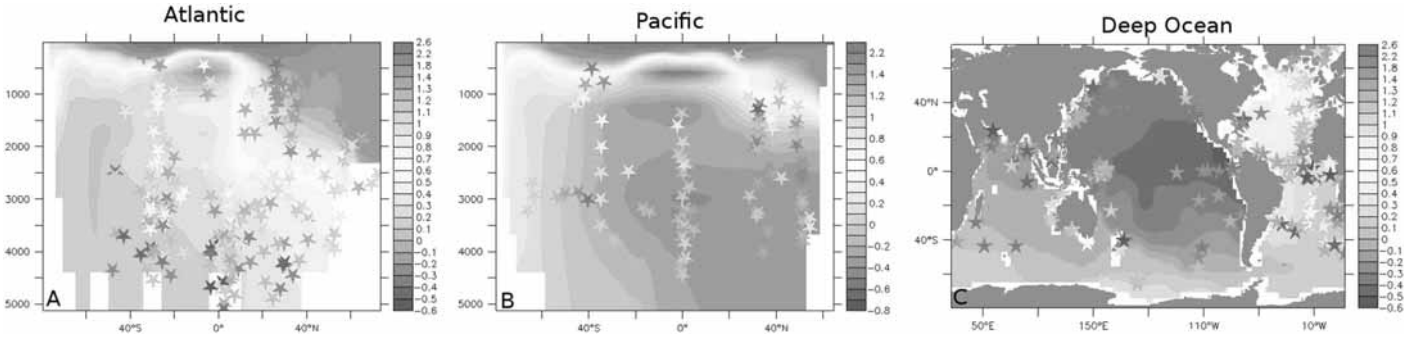

Figure 6. Best fit between simulated and proxy LGM δ^{13}C. δ^{13}C (‰) zonally averaged over (a) the Atlantic and (b) Pacific oceans as well as (c) in the deepest ocean layer for a simulation with weak NADW, very weak AABW, and a 426 Gt C lower LGM terrestrial carbon content (V3LNAwSOwSHWw ⋆). Symbols represent paleoproxy records [*Peterson et al.*, 2014].

3.3. Antarctic Bottom Water Formation at the LGM

As seen in Figure 1b, negative correlations between simulated and benthic $\Delta\delta^{13}$C are also obtained for experiments with strong AABW (SOs, △). Strong AABW leads to positive δ^{13}C anomalies in the deep Southern and Pacific Oceans while inducing negative δ^{13}C anomalies in the North Atlantic at intermediate depths [*Menviel et al.*, 2015]. Positive $\Delta\delta^{13}$C in the deep ocean are primarily due to a reduction in respired carbon. The LGM simulation featuring strong AABW transport and including a 320 Gt C terrestrial carbon change (V3LNAwSOs △) thus displays less negative $\Delta\delta^{13}$C (Figure 2c) and less respired carbon (Figure 4c) in the deep ocean than simulations with a weaker AABW transport (e.g., Figures 2e and 4e).

Paleoproxy data suggest that δ^{13}C increased in the intermediate North Atlantic and decreased in the deep Atlantic, particularly south of 20°N. As such an increased vertical δ^{13}C gradient is also obtained when AABW is reduced [*Menviel et al.*, 2015]; experiments in which both NADW and AABW are weakened (Figures 2e and 2f) lead to a better fit with proxy $\Delta\delta^{13}$C. Our simulations further show that the weaker the AABW transport in the Indo-Pacific basin, the lower $\Delta\delta^{13}$C in the deep Pacific and Indian [*Menviel et al.*, 2015], which aligns well with the proxy data (Figures 1 and 2 and Table 1). In addition, as the surface ocean δ^{13}C rarely reaches equilibrium with the atmosphere, air-sea gas exchange has a significant impact on both oceanic and atmospheric δ^{13}C. Weakening of the Southern Hemispheric Westerlies slows the $\delta^{13}CO_2$ air-sea exchange, with an effect to raise atmospheric $\delta^{13}CO_2$ and decrease oceanic δ^{13}C [*Menviel et al.*, 2015]. The best match between simulated and proxy δ^{13}C ($R = 0.77$) is thus obtained for weak NADW and very weak AABW associated with a 20% reduction of the Southern Hemispheric westerlies (V3LNAwSOwSHWw ⋆ in Figures 1, 2f, and 6).

The fit between simulated and reconstructed ventilation ages also improves in both the Atlantic and Pacific basins with reduced AABW transport (Figures 5e and 5f). Indeed, reconstructed ventilation ages suggest a poorly ventilated deep South Atlantic and Pacific [*Sikes et al.*, 2000; *Barker et al.*, 2010; *Skinner et al.*, 2010; *Ronge et al.*, 2016], which can only be simulated with a weak AABW transport. In the deep Pacific basin, there is, however, a fairly large spread of LGM ventilation ages (∼1500 years) and sparse data coverage below 3000 m water depth.

3.4. North Pacific Intermediate Water Formation at the LGM

Data from the North Pacific also places constraints on oceanic circulation changes. North Pacific δ^{13}C records from 1000 to 2000 m water depth display negative $\Delta\delta^{13}$C in agreement with most simulations, except for experiments in which NADW is shut down (Figure 2). With a closed Bering Strait during the last glacial, cessation of NADW leads to strong (∼12 Sv) formation of North Pacific Intermediate Water (NPIW) in our simulations [*Matsumoto et al.*, 2002; *Okazaki et al.*, 2010; *Menviel et al.*, 2011], which results in positive $\Delta\delta^{13}$C in the intermediate North Pacific. The simulation that leads to the best agreement with paleoproxy records (V3LNAwSOwSHWw ⋆) features NPIW with a maximum overturning strength of 8 Sv reaching down to ∼1400 m water depth (Figure 6b).

The set of LGM simulations suggest that there should be a steep vertical gradient in ventilation ages at the depth boundary between NPIW and southern-sourced waters in the North Pacific (Figure 5). LGM simulations featuring cessation of NADW formation (e.g., V3LNAoff) are associated with relatively strong (∼12 Sv) NPIW formation reaching down to a water depth of ∼2000 m (Figure 2b). These simulations display a large

ventilation age gradient at ~2000 m depth in the North Pacific (Figure 5b), in contrast with estimated ventilation ages from the intermediate North Pacific, which display a large vertical gradient between 1000 and 1500 m water depth. (Figures 5d–5f).

We therefore conclude that NPIW formation during the LGM was most likely relatively weak (6–8 Sv) and limited to the upper 1500 m. This indicates limited ventilation of the deep ocean via the North Pacific during the LGM.

3.5. Iron Fertilization Impact on Oceanic $\delta^{13}C$

In the LGM experiments the simulated export production decreases south of the current Antarctic Polar Front in agreement with a compilation of paleoproxy records [*Kohfeld et al.*, 2005] (Figure S6). However, since the impact of iron fertilization is not included in our simulations, export production also decreases north of the Antarctic Polar Front, opposite to paleoreconstructions and particularly in the South Atlantic sector. To investigate the potential impact of iron fertilization on oceanic $\delta^{13}C$, additional LGM experiments were performed in which export production was enhanced between 56°S and 36°S (V3LNAwGR ○, Table 1). A 30% increase in Southern Ocean export production, compared to LGM experiments with weaker NADW (V3LNAw ●), only leads to a 0.05‰ $\delta^{13}C$ decrease in the deep Southern Ocean (Figure S7). The weak impact of iron fertilization on deep ocean $\delta^{13}C$ is further confirmed by experiments performed with the Bern3D Earth System model [*Menviel et al.*, 2012]. Thus, while changes in Southern Ocean nutrient utilization might have played a significant role in controlling past atmospheric CO_2, their impact on setting the glacial oceanic $\delta^{13}C$ distribution was relatively small [*Tagliabue et al.*, 2009; *Bouttes et al.*, 2011; *Menviel et al.*, 2012; *Schmittner and Somes*, 2016].

4. Discussion and Conclusions

By refining earlier work [*Shackleton*, 1977; *Duplessy et al.*, 1988; *Bird et al.*, 1994], recent studies [*Ciais et al.*, 2012; *Peterson et al.*, 2014] estimate a 330 to 694 Gt C land carbon increase during the last deglaciation. Our results show that among simulations that display significant correlations with the proxy, those with a terrestrial carbon change greater than 500 Gt C between the LGM and the Holocene would either underestimate the positive $\delta^{13}C$ anomalies in the intermediate North Atlantic or significantly overestimate the negative $\delta^{13}C$ anomalies in the deep North Pacific. Our study, based on a consistent three-dimensional and dynamical framework, thus suggests that the LGM terrestrial carbon was 378 ± 88 Gt C (2σ) lower than during the late Holocene. Estimates of LGM terrestrial carbon could be refined by better constraining the LGM terrestrial $\delta^{13}C$ value as well as deep Pacific $\delta^{13}C$. Considering a ~90 ppmv (1 ppmv~2.12 Gt C) drop in atmospheric CO_2 at the LGM, the ocean must gain an extra ~570 Gt C from the change in atmospheric and terrestrial carbon reservoirs.

Very low deep South Atlantic benthic $\delta^{13}C$ values remained unexplained (Figure 6) but could partially be affected by the influence of ^{13}C-depleted phytodetritus layers [*Mackensen et al.*, 1993]. Previous studies [*Spero et al.*, 1997; *Bemis et al.*, 2000] have suggested that planktonic foraminiferal $\delta^{13}C$ might also be influenced by the ambient carbonate ion content, calcification temperature, and physiological processes such as respiration and symbiont photosynthesis [*Spero et al.*, 1991; *Hesse et al.*, 2014], but little is known about their effects on benthic foraminiferal $\delta^{13}C$. Considering similar global mean deep water carbonate ions content [*Yu et al.*, 2013] between the LGM and the Holocene and the lack of symbionts associated with *Cibicidoides* spp., benthic $\delta^{13}C$ appears to reliably record deep water signals. Further work is needed to better constrain secondary factors affecting benthic $\delta^{13}C$ and reasons responsible for the very low benthic $\delta^{13}C$ observed in the glacial deep South Atlantic.

We performed 28 millennial-scale simulations with the LOVECLIM Earth System Model of Intermediate Complexity to explore the influence of changes in deep water mass formation (rate and volumetric extent) on the oceanic $\delta^{13}C$ distribution during the LGM. We find that only a reduced deep ocean ventilation is consistent with the reconstructed patterns of $\Delta\delta^{13}C$ and ocean ventilation ages. As in any model study, our results depend on the underlying physics of the model. Even though regional climate responses to changes in freshwater input and wind stress might be model dependent and our large ensemble of simulations may still not capture all potential circulation modes under glacial conditions, the major known water masses are systematically varied in this study, bolstering the robustness of our conclusions. Different circulation states are explored to the extent possible within the physically and biogeochemically self-consistent settings of a dynamic coupled ocean-atmosphere model. Our findings are further supported by results obtained with the Bern3D dynamic ocean model and the published analyses from other paleoproxy records [*Lynch-Stieglitz et al.*, 1999, 2006; *Marchitto and Broecker*, 2006; *Jaccard et al.*, 2009; *Howe et al.*, 2016].

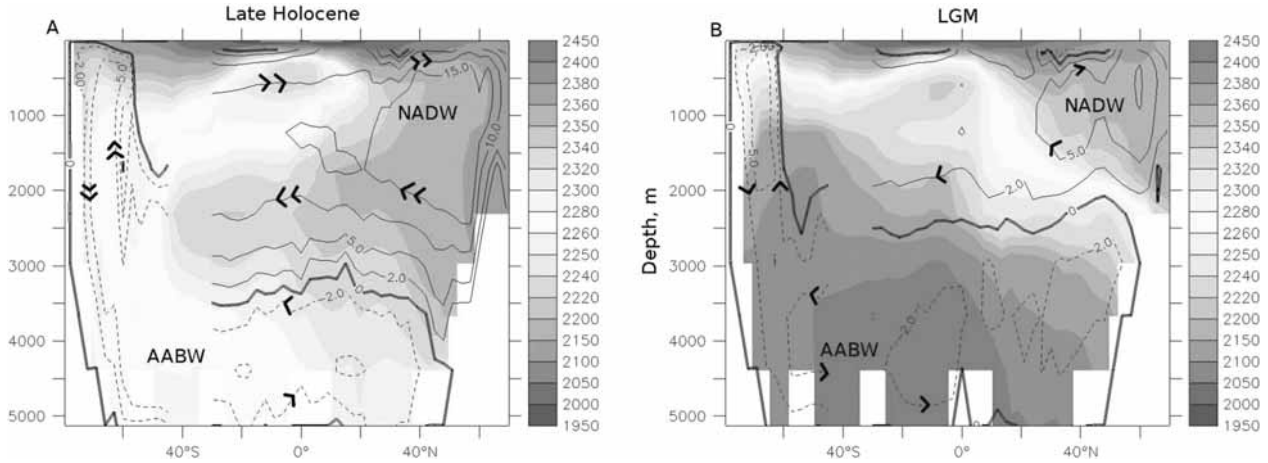

Figure 7. Deep ocean carbon sequestration resulting from a weakened oceanic circulation. Compared to (a) the late Holocene, NADW and AABW formation at (b) the LGM (V3LNAwSOwSHWw ⋆) were weakened with a shoaling of their boundary. The color shading shows zonal mean dissolved inorganic carbon content (μmol/L) in the Atlantic. Overlaid contours are the Atlantic (north of 30°S) and global (south of 30°S) meridional overturning stream function (Sv).

In detail, the spatial distribution of $\Delta\delta^{13}C$ as well as ventilation ages suggest that NADW was weaker and shallower during the LGM, in agreement with previous paleodata-model comparisons [*Tagliabue et al.*, 2009; *Hesse et al.*, 2011; *Menviel et al.*, 2012; *Schmittner and Somes*, 2016]. The shift from positive to negative $\Delta\delta^{13}C$ in the North Atlantic occurs at about 2000–2500 m water depth, delineating the boundary between northern-sourced waters above that depth and southern-sourced waters below. Only simulations in which NADW weakens and shoals to that water depth display such an anomaly pattern (Figure 2). While the dynamics of our model does not allow us to test the possibility that NADW was at the same time shallower and stronger at the LGM, we note that the correlation between model and proxy increases as NADW weakens. Negative $\Delta\delta^{13}C$ in the deep North Atlantic are due to reduced ventilation from northern-sourced waters and associated greater penetration of southern-sourced waters, while positive $\Delta\delta^{13}C$ in the intermediate North Atlantic results from a combination of longer residence time at the surface, greater ^{13}C fractionation due to lower SST, and weaker advection of intermediate depth equatorial waters to the North Atlantic [*Menviel et al.*, 2015]. LGM Cd/Ca in the Atlantic basin further suggests low nutrient content above 2500 m water depth in the North Atlantic and high nutrient content below [*Marchitto and Broecker*, 2006], best represented by a weak and shallow NADW (Figure 3). A weaker and shallower NADW is also necessary, but not sufficient, to explain the relatively good ventilation of North Atlantic intermediate-depth water and poor ventilation of North Atlantic deep waters (Figure 5) [*Freeman et al.*, 2016].

Greater neodymium isotope (ϵ_{Nd}) values at the LGM than during the Holocene in the Atlantic below 2500 water depth [*Böhm et al.*, 2015; *Howe et al.*, 2016] further indicate a shallower boundary between NADW and AABW at the LGM [*Friedrich et al.*, 2014]. Our results, however, contrast with relatively low $^{231}Pa/^{230}Th$ values in the Atlantic basin at the LGM [*Lippold et al.*, 2012; *Böhm et al.*, 2015], which have been interpreted as indicating a relatively strong NADW transport. Our results indicate that a LGM state featuring a maximum overturning stream function greater than ~19 Sv in the North Atlantic would lead to negative $\Delta\delta^{13}C$ in the upper ~1500 m of the North Atlantic in contrast with benthic $\delta^{13}C$ data.

In addition, we find that weaker AABW, either through buoyancy forcing or reduced intensity of Southern Hemispheric Westerlies, improves the fit between model and paleoproxy data in all ocean basins. Through reduced deep ocean ventilation, weaker AABW decreases deep ocean $\delta^{13}C$ while increasing surface $\delta^{13}C$ and atmospheric $\delta^{13}CO_2$, thus leading to a steeper oceanic vertical $\delta^{13}C$ gradient. Weaker AABW transport is consistent with high ventilation ages in the deep South Atlantic and Pacific during the last ice age [*Sikes et al.*, 2000; *Galbraith et al.*, 2007; *Skinner et al.*, 2010; *Sarnthein et al.*, 2013; *Skinner et al.*, 2015; *Ronge et al.*, 2016] (Figure 5) as well as higher ϵ_{Nd} values in the deep Atlantic ocean [*Friedrich et al.*, 2014; *Howe et al.*, 2016]. Furthermore, weaker AABW at the LGM could potentially explain *Gebbie* [2014]'s results, which suggest a relatively small reduction in the proportion of northern-sourced waters in the glacial Atlantic, although past Atlantic meridional overturning circulation changes surely require further studies. A weaker AABW formation rate at the LGM could result from the presence of grounded ice over today's main AABW formation regions

such as the Ross and Weddell Seas [*Pollard and DeConto*, 2009; *Golledge et al.*, 2014]. Weakened or equatorward shifted Southern Hemispheric Westerlies at the LGM [*Toggweiler et al.*, 2006; *Menviel et al.*, 2008; *Tschumi et al.*, 2011] would also reduce AABW formation and air-sea gas exchange in the Southern Ocean. Our simulations further suggest small oceanic circulation changes in the North Pacific at the LGM compared to the late Holocene, with a best estimate of a NPIW transport of ~8 Sv reaching down to 1000–1500 m water depth.

The overall reduced oceanic ventilation at the LGM enhances the efficiency of the oceanic biological pump [*Toggweiler*, 1999; *Sigman and Boyle*, 2000; *Ito and Follows*, 2005; *Tschumi et al.*, 2011; *Menviel et al.*, 2014], by enhancing the storage of respired carbon in the ocean interior without causing anoxia (Figures 4, S9, and S10). In our simulations, weakened NADW formation raises deep ocean (≥2600 m depth) carbon storage by 216 Gt C, or by 504 Gt C for a concomitant AABW weakening (Figures 7 and S8). Therefore, reduced deep ocean ventilation during the glaciation would contribute to lowering atmospheric CO_2, with important implications for past carbon cycle and climate changes.

Acknowledgments
We thank the Editor Ellen Thomas as well as two anonymous reviewers for their helpful comments. This project was supported by the Australian Research Council. L. Menviel, and M. England acknowledge funding from the Australian Research Council grants DE150100107 and FL100100214, respectively. J. Yu acknowledges funding from the Australian Research Council grants FT140100993, DP140101393, K. Meissner acknowledges support from a UNSW Faculty of Science Silverstar award. F.J. acknowledges funding by the Swiss National Science Foundation. LOVECLIM experiments were performed on a computational cluster owned by the Faculty of Science of the University of New South Wales, Sydney, Australia. Bern3D experiments were performed on a computational cluster owned by the Department of Environmental Physics of the University of Bern, Switzerland. Results of the modeling experiments are available at http://dx.doi.org/10.4225/41/58192cb8bff06 and under LGMc13 at http://climate-cms.unsw.wikispaces.net/ARCCSS+published+datasets.

References

Abe-Ouchi, A., T. Segawa, and F. Saito (2007), Climatic conditions for modelling the Northern Hemisphere ice sheets throughout the Ice Age cycle, *Clim. Past*, *3*, 423–438.

Barker, S., G. Knorr, M. J. Vautravers, P. Diz, and L. C. Skinner (2010), Extreme deepening of the Atlantic overturning circulation during deglaciation, *Nat. Geosci.*, *3*, 567–571.

Bé, M., V. Chisté, C. Dulieu, X. Mougeot, V. Chechev, F. Kondev, A. Nichols, X. Huang, and B. Wang (2013), *Table of Radionuclides (Comments on Evaluations), Monographie BIPM-5*, vol. 7, Bureau International des Poids et Mesures, Pavillon de Breteuil, Sèvres, France.

Bemis, B. E., H. J. Spero, D. W. Lea, and J. Bijma (2000), Temperature influence on the carbon isotopic composition of Globigerina bulloides and Orbulina universa (planktonic foraminifera), *Mar. Micropaleontol.*, *38*, 213–228.

Bird, M. I., J. Lloyd, and G. D. Farquhar (1994), Terrestrial carbon storage at the LGM, *Nature*, *371*, 566.

Böhm, E., J. Lippold, M. Gutjahr, M. Frank, P. Blaser, B. Antz, J. Fohlmeister, N. Frank, M. B. Andersen, and M. Deininger (2015), Strong and deep Atlantic meridional overturning circulation during the last glacial cycle, *Nature*, *517*, 73–76.

Bouttes, N., D. Paillard, D. M. Roche, V. Brovkin, and L. Bopp (2011), Last Glacial Maximum CO_2 and $\delta^{13}C$ successfully reconciled, *Geophys. Res. Lett.*, *38*, L02705, doi:10.1029/2010GL044499.

Brovkin, V., A. Ganopolski, and Y. Svirezhev (1997), A continuous climate-vegetation classification for use in climate-biosphere studies, *Ecol. Modell.*, *101*, 251–261.

Burke, A., and L. F. Robinson (2012), The Southern Ocean's role in carbon exchange during the last deglaciation, *Science*, *335*, 557–561.

Ciais, P., et al. (2012), Large inert carbon pool in the terrestrial biosphere during the Last Glacial Maximum, *Nat. Geosci.*, *5*, 74–79, doi:10.1038/NGE01324.

Cook, M. S., and L. D. Keigwin (2015), Radiocarbon profiles of the NW Pacific from the LGM and deglaciation: Evaluating ventilation metrics and the effect of uncertain surface reservoir ages, *Paleoceanography*, *30*, 174–195, doi:10.1002/2014PA002649.

Curry, W. B., and D. W. Oppo (2005), Glacial water mass geometry and the distribution of $\delta^{13}C$ of ΣCO_2 in the western Atlantic Ocean, *Paleoceanography*, *20*, PA1017, doi:10.1029/2004PA001021.

Davies-Walczak, M., A. C. Mix, J. S. Stoner, J. R. Southon, M. Cheseby, and C. Xuan (2014), Late Glacial to Holocene radiocarbon constraints on North Pacific Intermediate Water ventilation and deglacial atmospheric CO_2 sources, *Earth Planet. Sci. Lett.*, *397*, 57–66.

Duplessy, J. C., N. J. Shackleton, R. G. Fairbanks, L. Labeyrie, D. Oppo, and N. Kallel (1988), Deepwater source variations during the last climate cycle and their impact on the global deepwater circulation, *Paleoceanography*, *3*, 343–360.

Francois, L. M., Y. Goddéris, P. Warnant, G. Ramstein, N. de Noblet, and S. Lorenz (1999), Carbon stocks and isotopic budgets of the terrestrial biosphere at mid-Holocene and last glacial maximum times, *Chem. Geol.*, *159*, 163–189.

Freeman, E., L. C. Skinner, A. Tisserand, T. Dokken, A. Timmermann, L. Menviel, and T. Friedrich (2015), An Atlantic Pacific ventilation seesaw across the last deglaciation, *Earth Planet. Sci. Lett.*, *424*, 237–244.

Freeman, E., L. C. Skinner, C. Waelbroeck, and D. Hodell (2016), Radiocarbon evidence for enhanced respired carbon storage in the Atlantic at the Last Glacial Maximum, *Nat. Commun.*, *7*, 11998, doi:10.1038/ncomms11998.

Freeman, K. H., and J. M. Hayes (1992), Fractionation of carbon isotopes by phytoplankton and estimates of ancient CO_2 levels, *Global Biogeochem. Cycles*, *6*, 185–198.

Friedrich, T., A. Timmermann, T. Stichel, and K. Pahnke (2014), Ocean circulation reconstructions from ϵ_{Nd}: A model-based feasibility study, *Paleoceanography*, *29*, 1003–1023, doi:10.1002/2014PA002658.

Galbraith, E. D., S. L. Jaccard, T. F. Pedersen, D. M. Sigman, G. H. Haug, M. Cook, J. R. Southon, and R. Francois (2007), Carbon dioxide release from the North Pacific abyss during the last deglaciation, *Nature*, *449*, 890–894.

Gebbie, G. (2014), How much did Glacial North Atlantic Water shoal?, *Paleoceanography*, *19*, 190–209, doi:10.1002/2013PA002557.

Gherardi, J. M., L. Labeyrie, S. Nave, R. Francois, J. F. McManus, and E. Cortijo (2009), Glacial-interglacial circulation changes inferred from $^{231}Pa/^{230}Th$ sedimentary record in the North Atlantic region, *Paleoceanography*, *24*, PA2204, doi:10.1029/2008PA001696.

Golledge, N. R., L. Carter, L. Menviel, C. J. Fogwill, M. H. England, G. Cortese, and R. H. Levy (2014), Antarctic contribution to meltwater pulse 1A from reduced Southern Ocean overturning, *Nat. Commun.*, *5*, 5107, doi:10.1038/ncomms6107.

Gong, X., X. Zhang, G. Lohmann, W. Wei, X. Zhang, and M. Pfeiffer (2015), Higher Laurentide and Greenland ice sheets strengthen the North Atlantic Ocean circulation, *Clim. Dyn.*, *45*, 139–150, doi:10.1007/s00382-015-2502-8.

Goosse, H., et al. (2010), Description of the Earth system model of intermediate complexity LOVECLIM version 1.2, *Geosci. Model Dev.*, *3*, 603–633.

Hesse, T., M. Butzin, T. Bickert, and G. Lohmann (2011), A model-data comparison of $\delta^{13}C$ in the glacial Atlantic Ocean, *Paleoceanography*, *26*, PA3220, doi:10.1029/2010PA002085.

Hesse, T., D. Wolf-Gladrow, G. Lohmann, J. Bijma, A. Mackensen, and R. E. Zeebe (2014), Modelling $\delta^{13}C$ in benthic foraminifera: Insights from model sensitivity experiments, *Mar. Micropaleontol.*, *112*, 50–61.

Howe, J. N. W., A. M. Piotrowski, T. L. Noble, S. Mulitza, C. M. Chiessi, and G. Bayon (2016), North Atlantic deep water production during the Last Glacial Maximum, *Nat. Commun.*, *7*, 11765, doi:10.1038/ncomms11765.

Ito, T., and M. J. Follows (2005), Preformed phosphate, soft tissue pump and atmospheric CO_2, *J. Mar. Res.*, *63*, 813–839.

Jaccard, S. L., E. D. Galbraith, D. M. Sigman, G. H. Haug, R. Francois, T. F. Pedersen, P. Dulski, and H. R. Thierstein (2009), Subarctic Pacific evidence for a glacial deepening of the oceanic respired carbon pool, *Earth Planet. Sci. Lett.*, *277*, 156–165.

Joos, F., S. Gerber, I. C. Prentice, B. L. Otto-Bliesner, and P. J. Valdes (2004), Transient simulations of Holocene atmospheric carbon dioxide and terrestrial carbon since the Last Glacial Maximum, *Global Biogeochem. Cycles*, *18*, GB2002, doi:10.1029/2003GB002156.

Keigwin, L. D. (2004), Radiocarbon and stable isotope constraints on Last Glacial Maximum and Younger Dryas ventilation in the western North Atlantic, *Paleoceanography*, *19*, PA4012, doi:10.1029/2004PA001029.

Keigwin, L. D., and M. A. Schlegel (2002), Ocean ventilation and sedimentation since the glacial maximum at 3 km in the western North Atlantic, *Geochem. Geophys. Geosyst.*, *3*(6), 1034, doi:10.1029/2001GC000283.

Kohfeld, K. C., C. Le Quere, S. Harrison, and R. Anderson (2005), Role of marine biology in glacial-interglacial CO_2 cycles, *Science*, *308*, 74–78.

Köhler, P., and H. Fischer (2004), Simulating changes in the terrestrial biosphere during the last glacial/interglacial transition, *Global Planet. Change*, *43*, 33–55.

Kovaltsov, G. A., A. Mishev, and I. G. Usoskin (2012), A new model of cosmogenic production of radiocarbon ^{14}C in the atmosphere, *Earth Planet. Sci. Lett.*, *337–338*, 114–120.

Lippold, J., Y. Luo, R. Francois, S. E. Allen, J. Gherardi, S. Pichat, B. Hickey, and H. Schulz (2012), Strength and geometry of the glacial Atlantic Meridional overturning circulation, *Nat. Geosci.*, *5*, 813–816.

Lund, D. C., A. C. Tessin, J. L. Hoffman, and A. Schmittner (2015), Southwest Atlantic water mass evolution during the last deglaciation, *Paleoceanography*, *30*, 477–494, doi:10.1002/2014PA002657.

Lynch-Stieglitz, J., W. B. Curry, and N. Slowey (1999), Weaker Gulf Stream in the Florida Straits during the Last Glacial Maximum, *Nature*, *402*, 644–648.

Lynch-Stieglitz, J., W. B. Curry, D. W. Oppo, U. S. Ninneman, C. D. Charles, and J. Munson (2006), Meridional overturning circulation in the South Atlantic at the Last Glacial Maximum, *Geochem. Geophys. Geosyst.*, *7*, Q10N03, doi:10.1029/2005GC001226.

Mackensen, A., H.-W. Hubberten, T. Bickert, G. Fischer, and D. K. Fütterer (1993), The $\delta^{13}C$ in benthic foraminiferal tests of Fontbotia wuellerstorfi (Schwager) relative to the $\delta^{13}C$ of dissolved inorganic carbon in Southern Ocean deep water: Implications for glacial ocean circulation models, *Paleoceanography*, *8*, 587–610.

Marchitto, T. M., and W. S. Broecker (2006), Deep water mass geometry in the glacial Atlantic Ocean: A review of constraints from the paleonutrient proxy Cd/Ca, *Geochem. Geophys. Geosyst.*, *7*, Q12003, doi:10.1029/2006GC001323.

Matsumoto, K., T. Oba, J. Lynch-Stiegliz, and H. Yamamoto (2002), Interior hydrography and circulation of the glacial Pacific Ocean, *Quat. Sci. Revi.*, *21*, 1693–1704.

Menviel, L., A. Timmermann, A. Mouchet, and O. Timm (2008), Climate and marine carbon cycle response to changes in the strength of the Southern Hemispheric westerlies, *Paleoceanography*, *23*, PA4201, doi:10.1029/2007PA001604.

Menviel, L., A. Timmermann, O. Timm, and A. Mouchet (2011), Deconstructing the last Glacial Termination: The role of millennial and orbital-scale forcings, *Quat. Sci. Rev.*, *30*, 1155–1172.

Menviel, L., F. Joos, and S. P. Ritz (2012), Modeling atmospheric CO_2, stable carbon isotope and marine carbon cycle changes during the last glacial-interglacial cycle, *Quat. Sci. Rev.*, *56*, 46–68.

Menviel, L., M. H. England, K. J. Meissner, A. Mouchet, and J. Yu (2014), Atlantic-Pacific seesaw and its role in outgassing CO_2 during Heinrich events, *Paleoceanography*, *29*, 58–70, doi:10.1002/2013PA002542.

Menviel, L., A. Mouchet, K. J. Meissner, F. Joos, and M. H. England (2015), Impact of oceanic circulation changes on atmospheric $\delta^{13}CO_2$, *Global Biogeochem. Cycles*, *29*, 1944–1961, doi:10.1002/2015GB005207.

Mook, W. G., J. C. Bommerson, and W. H. Staverman (1974), Carbon isotope fractionation between dissolved bicarbonate and gaseous carbon dioxide, *Earth Planet. Sci. Lett.*, *22*, 169–176.

Mouchet, A. (2011), A 3D model of ocean biogeochemical cycles and climate sensitivity studies, PhD thesis, Université de Liège, Liege, Belgium. [Available at http://hdl.handle.net/2268/98995.]

Mouchet, A. (2013), The ocean bomb radiocarbon inventory revisited, *Radiocarbon*, *55*, 1580–1594.

Mouchet, A., and L. M. Francois (1996), Sensitivity of a Global Oceanic Carbon Cycle Model to the circulation and to the fate of organic matter: Preliminary results, *Phys. Chem. Earth*, *21*, 511–516.

Munhoven, G. (2002), Glacial interglacial changes of continental weathering: Estimates of the related CO_2 and HCO_3^- flux variations and their uncertainties, *Global Planet. Change*, *33*, 155–176.

Okazaki, Y., A. Timmermann, L. Menviel, N. Harada, A. Abe-Ouchi, M. Chikamoto, A. Mouchet, and H. Asahi (2010), Deep water formation in the North Pacific during the Last Glacial Termination, *Science*, *329*, 200–204.

Otto-Bliesner, B. L., C. D. Hewitt, T. M. Marchitto, E. C. Brady, A. Abe-Ouchi, M. Crucifix, S. Murakami, and S. L. Weber (2007), Last Glacial Maximum ocean thermohaline circulation: PMIP2 model intercomparisons and data constraints, *Geophys. Res. Lett.*, *34*, L12706, doi:10.1029/2007GL029475.

Peterson, C. D., L. E. Lisiecki, and J. V. Stern (2014), Deglacial whole-ocean $\delta^{13}C$ change estimated from 480 benthic foraminiferal records, *Paleoceanography*, *29*, 549–563, doi:10.1002/2013PA002552.

De Pol-Holz, R., L. Keigwin, J. Southon, D. Hebbeln, and M. Mohtadi (2010), No signature of abyssal carbon in intermediate waters off Chile during deglaciation, *Nat. Geosci.*, *3*, 192–195, doi:10.1038/NGEO745.

Pollard, D., and R. M. DeConto (2009), Modelling West Antarctic ice sheet growth and collapse through the past five million years, *Nature*, *458*, 329–332.

Rae, J. W. B., M. Sarnthein, G. L. Foster, A. Ridgwell, P. M. Grootes, and T. Elliott (2014), Deep water formation in the North Pacific and deglacial CO_2 rise, *Paleoceanography*, *29*, 645–667, doi:10.1002/2013PA002570.

Ritz, S. P., T. F. Stocker, and S. Müller (2008), Modeling the effect of abrupt ocean circulation change on marine reservoir age, *Earth Planet. Sci. Lett.*, *268*, 202–211.

Ronge, T. A., R. Tiedemann, F. Lamy, P. Köhler, B. V. Alloway, R. De Pol-Holz, K. Pahnke, J. Southon, and L. Wacker (2016), Radiocarbon constraints on the extent and evolution of the South Pacific glacial carbon pool, *Nat. Commun.*, *7*, 11487, doi:10.1038/ncomms11487.

Rose, K. A., E. L. Sikes, T. P. Guilderson, P. Shane, T. M. Hill, R. Zahn, and H. J. Spero (2010), Upper-ocean-to-atmosphere radiocarbon offsets imply fast deglacial carbon dioxide release, *Nature*, *466*, 1093–1097, doi:10.1038/nature09288.

Roth, R., and F. Joos (2013), A reconstruction of radiocarbon production and total solar irradiance from the Holocene ^{14}C and CO_2 records: Implications of data and model uncertainties, *Clim. Past*, *9*, 1879–1909.

Sarnthein, M., K. Winn, S. J. A. Jung, J. C. Duplessy, L. Labeyrie, H. Erlenkeuser, and G. Ganssen (1994), Changes in east Atlantic deep water circulation over the last 30,000 years: Eight time slice reconstructions, *Paleoceanography*, *9*, 209–269.

Sarnthein, M., B. Schneider, and P. M. Grootes (2013), Peak glacial ^{14}C ventilation ages suggest major draw-down of carbon into the abyssal ocean, *Clim. Past*, *9*, 2595–2614.

Schmitt, J., et al. (2012), Carbon isotope constraints on the deglacial CO_2 rise from ice cores, *Science*, *136*, 711–714.

Schmittner, A., and C. J. Somes (2016), Complementary constraints from carbon (^{13}C) and nitrogen (^{15}N) isotopes on the glacial ocean's soft-tissue biological pump, *Paleoceanography*, *31*, 669–693, doi:10.1002/2015PA002905.
Shackleton, N. J. (1977), Carbon-13 in Uvigerina: Tropical rainforest history and the equatorial Pacific carbonate dissolution cycle, in *The Fate of Fossil Fuel CO_2 in the Oceans*, edited by N. R. Andersen and A. Malahoff, pp. 401–428, Plenum, New York.
Siani, G., E. Michel, R. De Pol-Holz, T. DeVries, F. Lamy, M. Carel, G. Isguder, F. Dewilde, and A. Lourantou (2013), Carbon isotope records reveal precise timing of enhanced Southern Ocean upwelling during the last deglaciation, *Nat. Commun.*, *4*, 2758, doi:10.1038/ncomms3758.
Siegenthaler, U., and K. O. Munnich (1981), $^{13}C/^{12}C$ fractionation during CO_2 transfer from air to sea, in *SCORE 16: Carbon Cycle Modelling*, edited by B. Bolin, pp. 249–257, Wiley, Chichester, England.
Sigman, D. M., and E. A. Boyle (2000), Glacial/interglacial variations in atmospheric carbon dioxide, *Nature*, *407*, 859–869.
Sikes, E. L., C. R. Samson, T. P. Guilderson, and W. R. Howard (2000), Old radiocarbon ages in the southwest Pacific Ocean during the last glacial period and deglaciation, *Nature*, *405*, 555–559.
Skinner, L. C., S. Fallon, C. Waelbroeck, E. Michel, and S. Barker (2010), Ventilation of the deep Southern Ocean and deglacial CO_2 rise, *Science*, *328*, 1147–1151.
Skinner, L. C., C. Waelbroeck, A. E. Scrivner, and S. Fallon (2014), Radiocarbon evidence for alternating northern and southern sources of ventilation of the deep Atlantic carbon pool during the last deglaciation, *Proc. Natl. Acad. Sci. U.S.A.*, *111*, 5480–5484.
Skinner, L. C., I. N. McCave, L. Carter, S. Fallon, A. E. Scrivner, and F. Primeau (2015), Reduced ventilation and enhanced magnitude of the deep Pacific carbon pool during the last glacial period, *Earth Planet. Sci. Lett.*, *411*, 45–52.
Spero, H. J., I. Lerche, and D. F. Williams (1991), Opening the carbon isotope "vital effect" black box 2, quantitative model for interpreting foraminiferal carbon isotope data, *Paleoceanography*, *6*, 639–655.
Spero, H. J., J. Bijma, D. W. Lea, and B. E. Bemis (1997), Effect of seawater carbonate concentration on foraminiferal carbon and oxygen isotopes, *Nature*, *390*, 497–500.
Tagliabue, A., L. Bopp, D. M. Roche, N. Bouttes, J.-C. Dutay, R. Alkama, M. Kageyama, E. Michel, and D. Paillard (2009), Quantifying the roles of ocean circulation and biogeochemistry in governing ocean carbon-13 and atmospheric carbon dioxide at the Last Glacial Maximum, *Clim. Past*, *5*, 695–706.
Thornalley, D. J. R., S. Barker, W. S. Broecker, H. Elderfield, and I. N. McCave (2011), The deglacial evolution of North Atlantic deep convection, *Science*, *331*, 202–205.
Toggweiler, J. R. (1999), Variation of atmospheric CO_2 by ventilation of the ocean's deepest water, *Paleoceanography*, *14*, 571–588.
Toggweiler, J. R., J. L. Russell, and S. R. Carson (2006), Midlatitude westerlies, atmospheric CO_2, and climate change during ice ages, *Paleoceanography*, *21*, PA2005, doi:10.1029/2005PA001154.
Tschumi, T., F. Joos, M. Gehlen, and C. Heinze (2011), Deep ocean ventilation, carbon isotopes, marine sedimentation and the deglacial CO_2 rise, *Clim. Past*, *7*, 771–800.
Ullman, D. J., A. N. Legrande, A. E. Carlson, F. S. Anslow, and J. M. Licciardi (2014), Assessing the impact of Laurentide Ice Sheet topography on glacial climate, *Clim. Past*, *10*, 487–507.
Vance, D., D. A. H. Teagle, and G. L. Foster (2009), Variable Quaternary chemical weathering fluxes and imbalances in marine geochemical budgets, *Nature*, *458*, 493–496.
Weber, S. L., S. S. Drijfhout, A. Abe-Ouchi, M. Crucifix, M. Eby, A. Ganopolski, S. Murakami, B. Otto-Bliesner, and W. R. Peltier (2007), The modern and glacial overturning circulation in the Atlantic Ocean in PMIP coupled model simulations, *Clim. Past*, *3*, 51–64.
Weldeab, S., T. Friedrich, A. Timmermann, and R. R. Schneider (2016), Strong middepth warming and weak radiocarbon imprints in the equatorial Atlantic during Heinrich 1 and Younger Dryas, *Paleoceanography*, *31*, 1070–1082, doi:10.1002/2016PA002957.
Wunsch, C. (2003), Determining paleoceanographic circulations, with emphasis on the Last Glacial Maximum, *Quat. Sci. Rev.*, *22*, 371–385.
Yu, J., H. Elderfield, and A. Piotrowski (2008), Seawater carbonate ion-$\delta^{13}C$ systematics and application to glacial-interglacial North Atlantic ocean circulation, *Earth Planet. Sci. Lett.*, *271*, 209–220.
Yu, J., R. F. Anderson, Z. Jin, J. W. B. Rae, B. N. Opdyke, and S. M. Eggins (2013), Responses of the deep ocean carbonate system to carbon reorganization during the Last Glacial-interglacial cycle, *Quat. Sci. Rev.*, *76*, 39–52.